AEROACOUSTICS OF HIGH SPEED RADIAL IMPELLERS

B. Karić, C. Scheit, A. Delgado, S. Becker

Uni. of Erlangen-Nuremberg, Inst. of Fluid Mechanics (LSTM), Cauerst. 4, 91058 Erlangen, Germany

Key words: turbomachines, centrifugal, aeroacoustics, efficiency, optimization

Abstract

In the present paper the flow inside radial impellers and the sound radiated from radial impellers with high rotating speed was investigated. For this purpose numerical and experimental techniques were applied. The aim was to get detailed information about the physical process leading to sound generation in radial impellers. The phenomena responsible for tonal noise and broadband noise were identified. Using this knowledge, design-guidelines were given to optimize the impeller in both aerodynamic and aeroacoustic way in order to obtain less noisy and more efficient centrifugal turbomachines.

Introduction

Turbomachines play a significant role in various industrial applications. The optimization of such machines is a very important process nowadays. In such a work one has to consider two phenomena, aerodynamics and aeroacoustics. The investigation of low noise fans has been carried out according to these phenomena. Over the past 10-15 years the computational power has emerged and holds promise to help with flow and noise prediction and to give deeper insight into their physics.

The machines investigated in the present work are radial fans with a tip Mach number of approximately 0.5. The main purpose of the work is to identify and connect the flow and design parameters responsible for the noise generation and efficiency reduction. Due to this, two different aspects have to be considered in the optimization process. The first aspect is to optimize the machines with respect to aerodynamics in order to reach better efficiency and to have a smaller consumption of energy. The second aspect is to find out sound sources responsible for the tonal and broadband components in the acoustic spectrum and based on this to reduce the sound pressure level generated and radiated from the machine.

Experimental Setup

In order to get an extensive data base for understanding the physics in the impeller flow and to validate the results from numerical simulations, experimental investigations were done. For that purpose a suction side chamber test rig was build. Experimental techniques include besides pressure rise and mass flow measurements also Laser-Doppler-anemometry (LDA) measurements at the impeller discharge. The complete setup can be seen in Figure 1. Additionally, in order to validate the results from the acoustic simulations the test rig was placed and the measurements were performed in the semi-anechoic room of the Technical Faculty, University of Erlangen-Nuremberg[1].
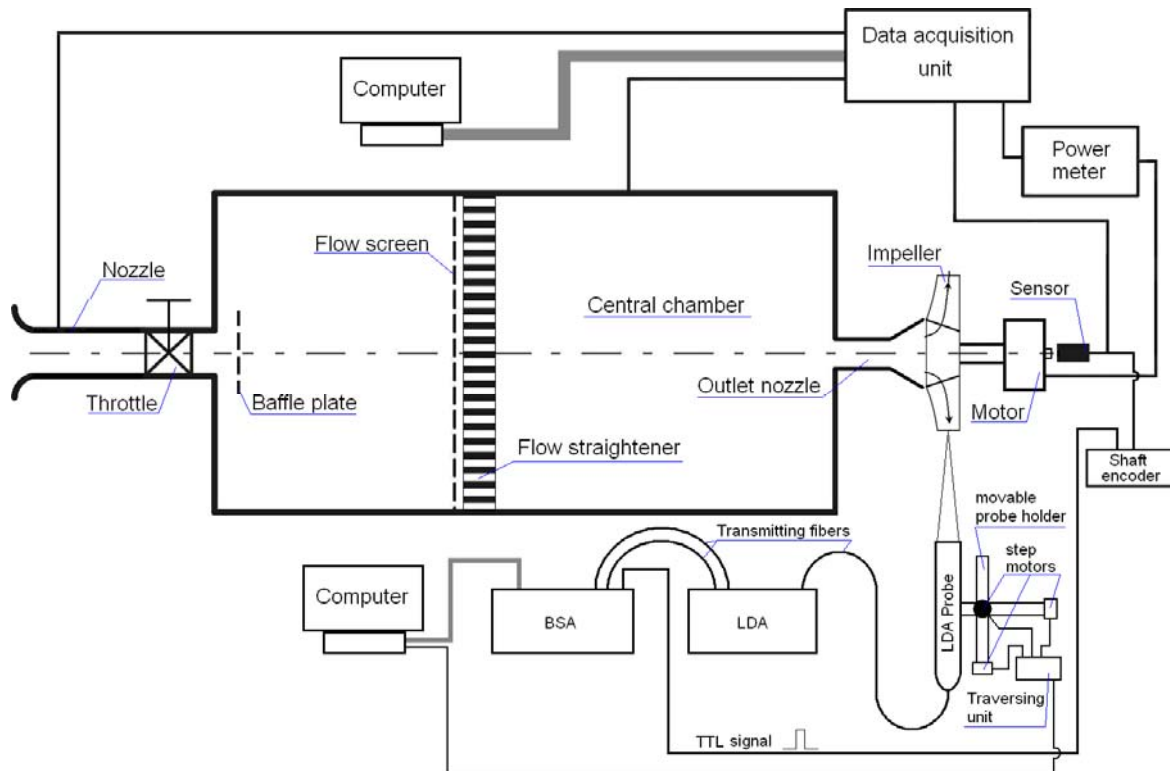
Figure 1: Schematic overview of the built test rig facility

The air was taken from the free atmosphere through the nozzle and the throttle which was also used to adjust the volume flow rate. In order to ensure straight flow a honey comb was placed centrally in the chamber. The speed of the motor, which was measured by a speed sensor, was automatically adjusted to the prescribed value by the computer and the power device. The pressure was obtained through a pressure sensor placed inside the chamber. Computational and experimental investigation of the chamber itself was done in order to obtain the system characteristics for various throttle positions.

The results obtained from CFD simulations were validated by measurements of the velocity field at the discharge of the impeller. In this purpose LDA was involved. For the velocity measurements a two-component back scattered LDA-system from Dantec was employed. Measurements were carried out on different axial and radial locations at the discharge of the impeller. In order to obtain the full 3D velocity field the co-ordinate transformation of the individual velocity samples had to be performed. All the velocity measurements were done phase resolved. A shaft encoder was placed at the end of the motor shaft and the impeller blades were synchronized with the shaft encoder unit. The phase had to be obtained very precisely because the aerodynamic phenomena of interest are occurring in the vicinity of the blade trailing edge and the exact position of it has to be known. Seeding particles were generated in the particle generator in which water with 10% of glycerine was mixed. Data acquisition was done by the burst spectrum analyzer which was connected to the computer. To control the whole data processing procedure, the software provided by Dantec was employed. Cyclic mode was used in order to resolve velocity information at the impeller discharge. For each measuring position a total number of 2.000.000 samples were collected. The data was then processed and statistically reduced by averaging the LDA measurements within increment of 1° of impeller shaft angle. After hardware validation and statistical processing an average of 3000 samples per radial position and per angular bin was obtained. Figure 2 shows a view of the LDA measurement setup in the test rig.
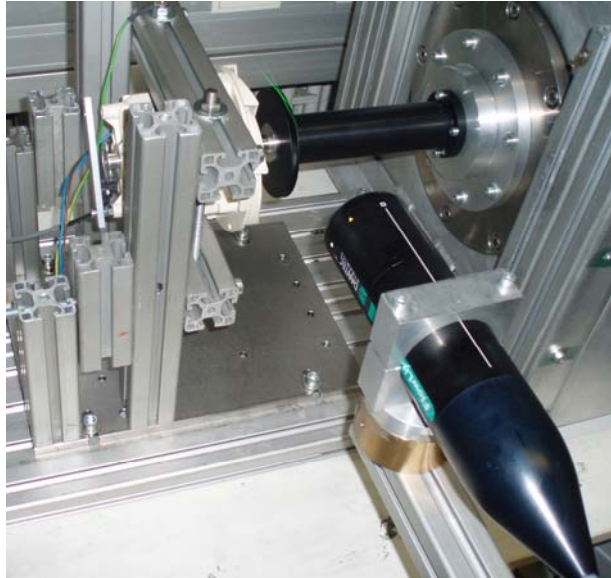
Figure 2: Discharge impeller velocity measurements

Computational method

The computational method was based on a hybrid approach. First, the compressible transient aerodynamic simulation was performed. The data from aerodynamic simulations was used as input for the acoustic simulation by using the Ffowcs-Williams and Hawkings (FW-H)[2] equation in order to compute the sound spectra in the far field. The input data set contains pressure, density and all three components of the velocity vector from the flow field in each time step.

A. Aerodynamic Formulation

In order to have a proper numerical simulation (CFD) of the machine, it was necessary to define the flow domain at first. The flow domain consisted of the impeller with all blade passages, the part of the test rig until the pressure sensors and the outlet domain. The complete model can be seen in Figure 3.
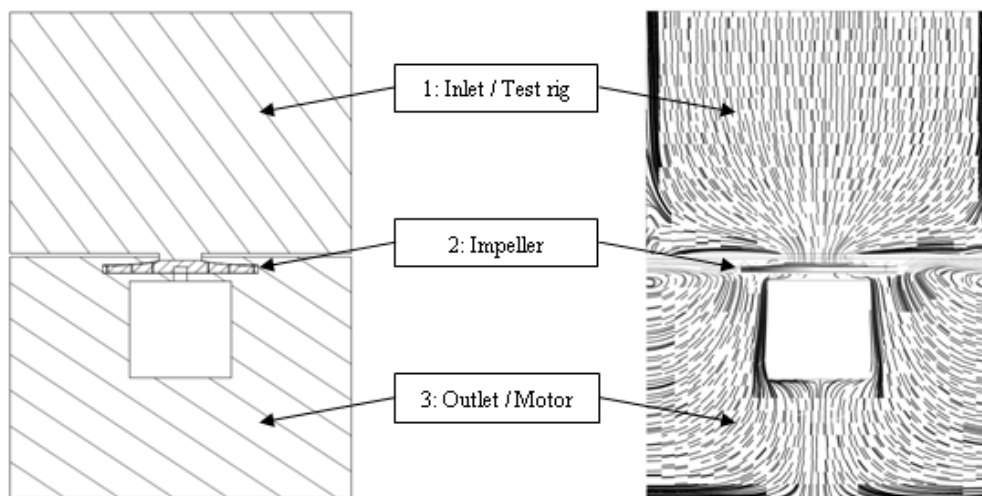

Figure 3: Flow domains: 1) test rig section, 2) impeller and 3) outlet domain

The reason to include the test rig and the outlet domain in the numerical simulation is that in such a way one can directly compare the results from the numerical simulation with

measurements at the test rig. The grids were generated with ANSYS ICEM 11.0. They consist of tetrahedral elements and of prism elements near walls. The grid was modeled with 2.340.567 elements, and 278.563 prism elements where used. These grid sizes resulted from a grid study in order to assure grid size independency.

To perform the numerical simulations, the commercial finite volume based Navier-Stokes solver ANSYS CFX 11.0 was used. The inlet boundary condition is mass flow rate and the outlet boundary is an opening boundary condition at ambient pressure. The prescribed rotational speeds for the impeller are obtained analytically from the torque-speed characteristic curve of the motor. Domains 1 and 3 are stationary. Hence, a multiple-frame-of-reference numerical calculation is performed. The interface between the different frames of reference is taken to be a Transient Rotor Stator General Connection Model.

The adopted turbulence model is the Shear Stress Transport Model (SST) of Menter[3]. It employs a turbulence/frequency-based model (k–ω) in the near-wall-region and a k-ε turbulence model in the bulk flow. A blending function ensures a smooth transition between the two models. The SST model performance has been studied in a large number of cases. In a NASA Technical Memorandum[4] SST was rated the most efficient and accurate model for aerodynamic applications.

In order to be sure of the convergence of the solution, besides of the mass, momentum, energy, turbulence kinetic energy and turbulence frequency residuals, monitor points were set on important quantities and locations. Monitor points were set at each boundary condition and interface to monitor the mass flow rate and pressure. Also the torque of the impeller was monitored. In such a way it was possible to assure that all flow domains were delivering properly stable converged mass flow rates and pressures and that the impeller torque also converged to a stable value. This is also an indication that the boundary conditions set are physically consistent.

B.   Aeroacoustic Formulation

The acoustic pressure p' radiated by the radial impeller is calculated by solving FW-H's equation in time domain. In the presented work the Formulation I of Farassat[5] is used, which can be written in the case of a stationary integration surface as:

$$p'(\vec{x},t) = p'_T(\vec{x},t) + p'_L(\vec{x},t) + p'_Q(\vec{x},t) \tag{1}$$

where p'_T is called thickness noise, p'_L loading noise and p'_Q is the quadrupole noise, which was not explicitly evaluated in the present work. Thickness and loading noise were calculated by integration over a porous surface S

$$4\pi p'_T(\vec{x},t) = \frac{\partial}{\partial t} \int_S \left[\frac{\rho_0 U_n}{R} \right]_{ret} dS \tag{2}$$

$$4\pi p'_L(\vec{x},t) = \frac{1}{a_0} \frac{\partial}{\partial t} \int_S \left[\frac{L_r}{R} \right]_{ret} dS + \int_S \left[\frac{L_r}{R} \right]_{ret} dS \tag{3}$$

with ρ_0 being the density and a_0 the speed of sound at ambient conditions, R the distance between surface source and the observer position and U_n, L_r as defined by Francescantonio[6]

27-4

$$U_n = \frac{\rho}{\rho_0} u_i \hat{n}_i$$

$$L_r = r_i \left(P_{ij} \hat{n}_j + \rho u_i u_n \right)$$

(4)

with u_i being the velocity vector, $\hat{n}_i$ the outward normal vector, P_{ij} the compressible stress tensor and r_i the distance vector between the surface source and the observer position. Subscript *ret* implies evaluation of the term at retarded time. Although the quardrupole noise is not explicitly calculated, all quadrupole sources inside the integration surface are implicitly taken into account. For the evaluation of the acoustic signal an advanced time method is used as presented by Casalino[7].

While for the retarded time algorithm the acoustic contribution of a surface element is calculated based on flow data in the past and for each surface element usually from a different simulation time step, this is not the case for the advanced time method. To calculate the acoustic contribution of a surface element only data from the actual time step is used and then the acoustic signal resulting from the surface source is extrapolated in time. As a consequence, the acoustic signal for a given time step at an observer point has to be calculated using various source (CFD) time steps. This is due to the fact that each surface element has a different runtime with respect to a fixed observer point position. As for the retarded time algorithm, the signal runtime between surface source and observer point in general is not a multiple of the discrete time step size Δt which hence requires for both algorithms an interpolation of the emitted (retarded time algorithm) or arriving (advanced time algorithm) signal. In contrast to the retarded time algorithm, for the advanced time algorithm still all simulation time steps are not available to do the interpolation. To use for instance a quadratic interpolation, one has to calculate first the arrival time of the signal, then calculate for this time step with respect to fixed interpolation points in time the interpolation weights and contribute to each interpolation point a part of the signal according to the interpolation weights. In case of a quadratic interpolation a contribution to three different interpolation points has to be calculated. As a consequence of this approach, three (source/CFD) time steps are needed to complete the calculation of the contribution of one surface source to an observer point to a given discrete arrival time step. This can also be seen from Fig. 4: in a) the interpolation using the advanced time approach is shown and in b) the same interpolation but for the retarded time approach. While for the advanced time approach three CFD time steps have to be evaluated in order to complete the interpolation for a given arrival time step, all data is directly available for the retarded time algorithm and hence interpolation can be done in only one step.
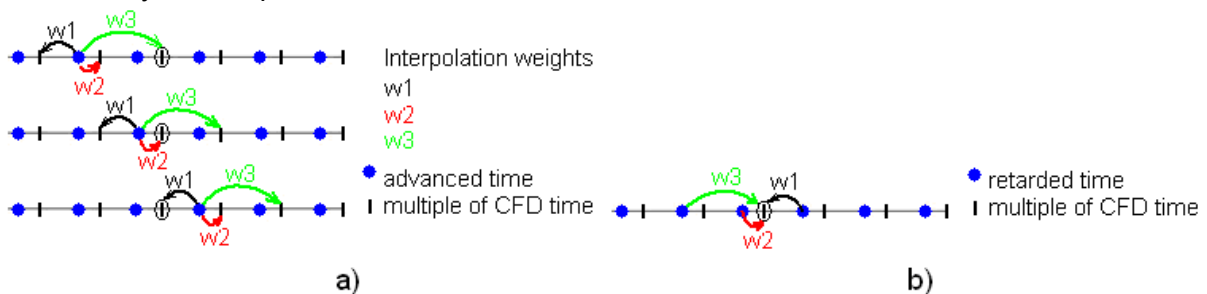

Figure 4: a) Interpolation in advanced time domain for three consecutive CFD time steps
b) Interpolation in retarded time domain

In the case presented here, using a stationary integration surface, the advanced time is calculated by:

$$t_{adv} = t + \frac{|r_i|}{a_0} \tag{5}$$

with t_{adv} being the signal arrival time and t the emission time (CFD/source time).

The interpolation in advanced time domain is carried out by the usage of Lagrange polynomials. The Lagrange polynomials of order n are defined by:

$$L_{n,k} = \prod_{i=0;i\neq k}^{n} \frac{\left(t_{CFD} - t_i\right)}{\left(t_k - t_i\right)} \tag{6}$$

where t_{CFD} is a multiple of the CFD time step size at which the acoustic signal should be evaluated, t_k and t_i are signal arrival times at which the acoustic contribution is known.

Using this definition, the interpolation by Lagrangian polynomials can be written as:

$$P\left(t_{CFD}\right) = \sum_{k=0}^{n} f\left(t_k\right) L_{n,k}\left(t_{CFD}\right) \tag{7}$$

where $f\left(t_k\right)$ is the known function value at time t_k. For the Ffowcs Williams-Hawkings formulation $f\left(t_k\right)$ is the value of one of the integrals at arrival time which will be interpolated to a multiple of the CFD time step t_{CFD}. The derivatives of integrals in Eq. 2 and 3 with respect to time are evaluated by a similar approach, but instead of the Lagrangian polynomials the according derivative with respect to t_{CFD} of the polynomials in Eq. 6 are taken. Currently, Lagrangian polynomials of order n=2 and n=3 are implemented. While interpolation in time is slightly more complicated using the advanced time approach, the advantage over retarded time is that for each acoustic post processing step only data from one CFD time step and therefore from only one file has to be taken. There are more advantages for moving control surfaces such that the layout of the algorithm is in favor for future extensions to moving control surfaces.

The integrals in Eq. 2 and 3 are evaluated using quadrature formulas and there are several available in the code. Since the CFD data is only provided at element corner nodes only a second order trapezoidal rule is used for the numerical evaluation of the integrals. In order to perform the integration, a transformation of quadrilateral surface elements to a reference element is performed. The normal vector of the element is evaluated only at the middle of the element. A similar approach but without calculating the transformation was applied for triangular surface elements. The overall order of the acoustic calculations is second order, which is corresponding to the order of the numerical calculations of the flow itself.

Results and Discussion

In order to fully understand the phenomena of the fluid flow and sound generation three different impellers were built, and the study of the blade shape on the hydraulic efficiency and noise production was done. The models are shown in Figure 5. Outer diameter of the impellers is 90mm. Impellers were designed to operate with the speed of 40.000min^{-1}.

Figure 5: Prototypes of impellers with wrap angles θ=120°, 150° and 228°

All three impellers have the same geometrical characteristics, like inlet and outlet dimensions and angles, except the blade shape between inlet and outlet. The first impeller has a wrap angle of 120 degree and very irregular shape of the blade. This was done to produce a very irregular flow inside it in order to analyze the influence of the large turbulent structures on the noise. The other two impellers have hydraulically optimized blade shape but the wrap angle is different. The blade shape was optimized in such a way that for a chosen blade shape the hydraulic efficiency is maximal comparing to the others in the process of an inverse design which has been deeply studied and done by Epple et al.[8]. This was performed in order to test the influence of the wrap angle on the tonal and broadband noise. Even though the pressure and efficiency characteristics of both impellers are nearly the same and very high, these two impellers show different acoustic behavior. The reason for that is that the flow field between the blades is different and the lengths of the blades are not the same in both configurations. One component with the tonal characteristic is present in the spectrum for which the vortex detachments and the eddy distribution in the flow channel between the blades are responsible. The vortex distribution is shown in Fig. 6.
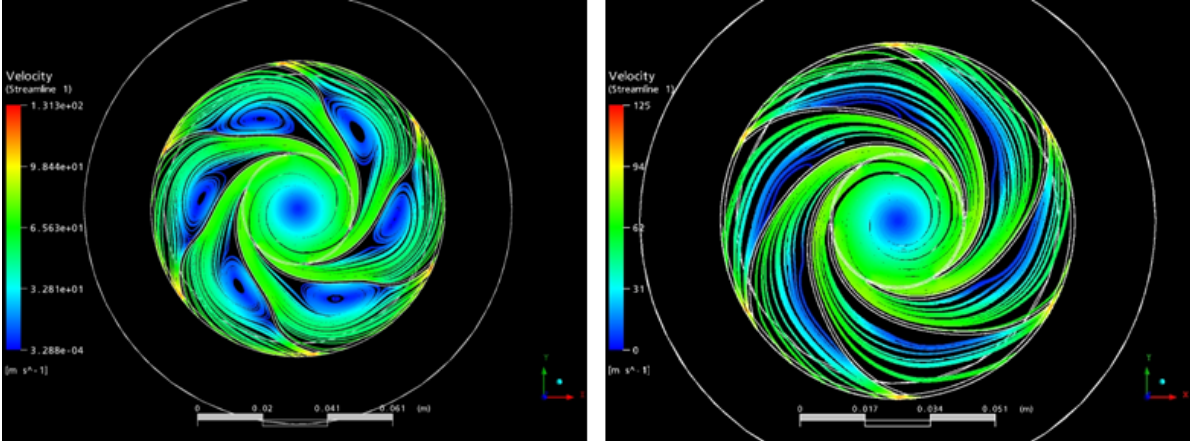

Figure 6: Large structures distributions θ=120° (irregular blade shape) and θ=150° (optimized blade shape)

The LDA measurements of all three impellers show good agreement between measurement and simulation. For the impeller with 150 degree wrap angle Figures 7 to 10 show the post processed data and its comparison with the simulation data for the radial and relative velocities as well as the distribution of the relative and absolute flow angles β_2 and α_2. The figures show the values obtained in the middle plain of the impeller at two different radial positions (1mm and 4 mm from the tip of the impeller). The values on the ordinate are scaled with the impeller tip speed which is in both cases 188.5 m/s. Since the number of blades is six, the value of $1/6$ on the abscissa represents the end of the blade passage and also the beginning of the adjacent one.
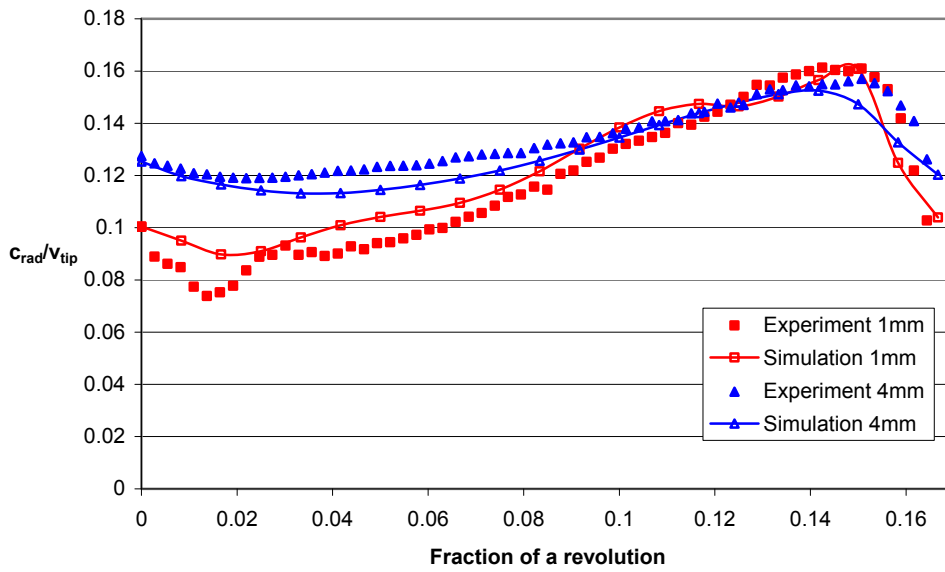
Figure 7: Radial velocity distribution at the impeller discharge
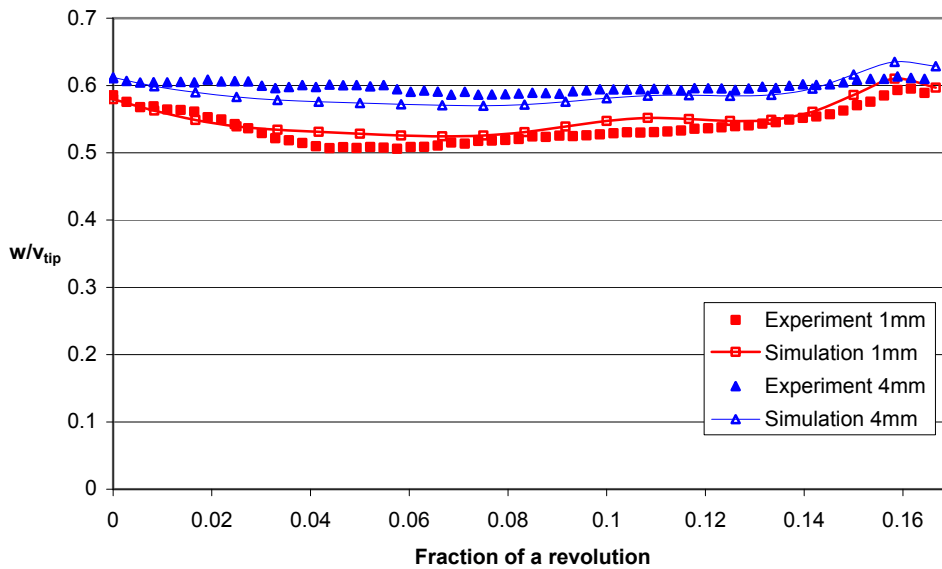

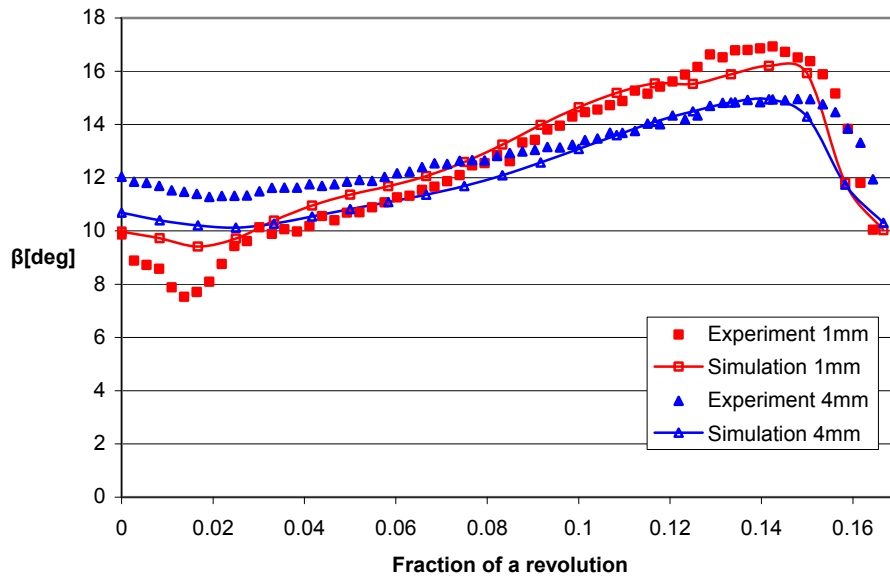Figure 8: Relative velocity distribution at the impeller discharge

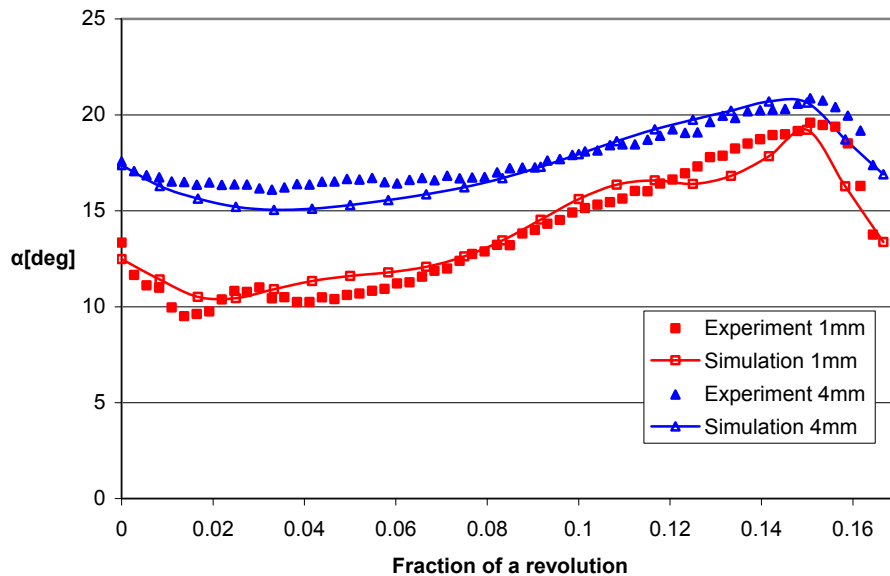Figure 9: Relative angle distribution at the impeller discharge

Figure 10: Absolute angle distribution at the impeller discharge

Figure 11 compares the spectra obtained by experiment and simulation of the impeller with 150 degree wrap angle. As one can see, a good agreement between both was obtained for broadband and tonal components. The slight frequency shift between the two peaks of the blade passage frequency is due to a small speed difference between simulation and experiment. The difference in the high frequency range between the experiment and simulation is due to the much longer measuring time in the experiment compared to the simulation time. The first tonal component is related to the vortex detachment, the second peak to the blade passage frequency and the third one to the second harmonic of the blade passage frequency.

In Figure 12 the sound pressure level (SPL) is plotted over the volume flow rate. Both, microphone measurements as well as simulation results for the impellers with 150 and 228 degree wrap angle are shown. A good agreement between measurement and simulation exists. As one can see, the impeller with 228 degree wrap angle is about 2 dB less noisy over the whole range. This result was obtained for both, experiment and simulation. Figure 13 shows the frequency spectra for 150 and 228 degree wrap angle of the simulation obtained by the FW-H method. The impeller with 150 degree wrap angle is louder than the impeller with 228 degree wrap angle over the whole frequency spectra.
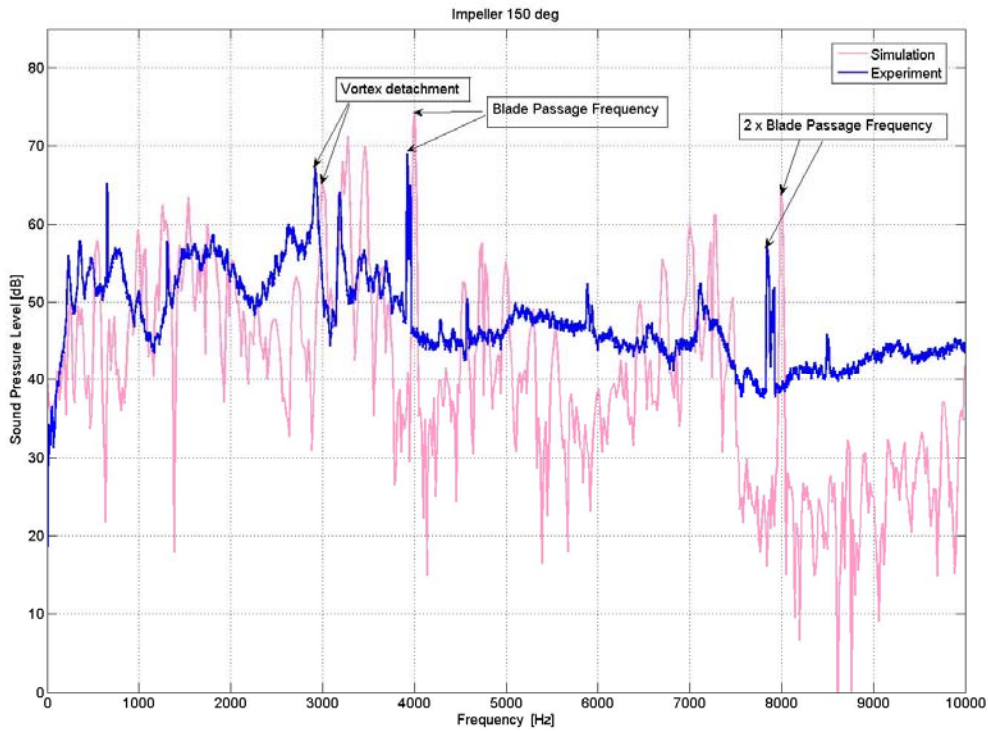

Figure 11: Radiated sound spectra from the radial impeller; Simulation and Experiment
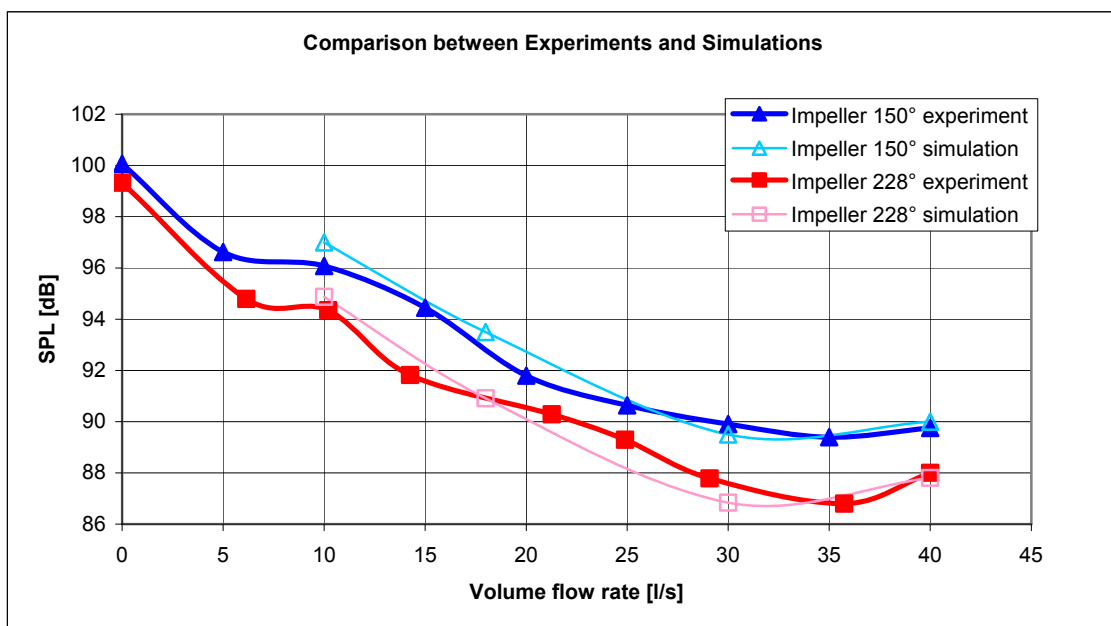

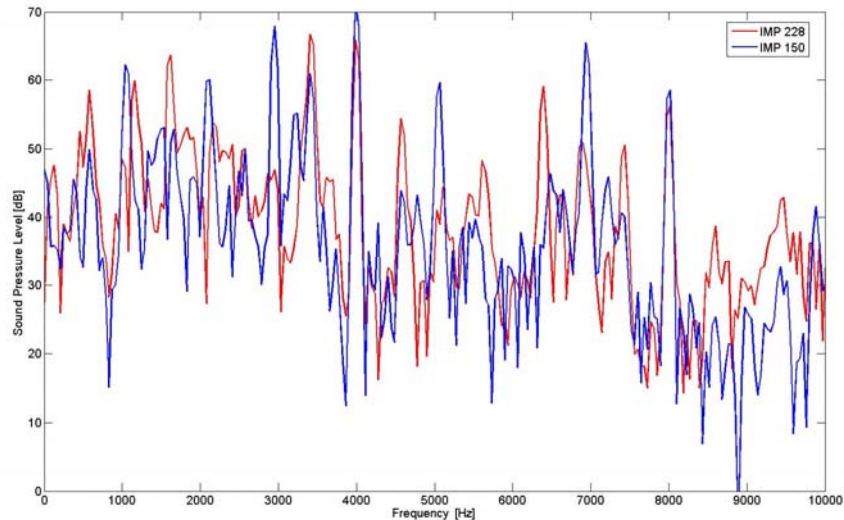Figure 12: SPL over volume flow rate for 150 and 228 degree wrap angle

Figure 13: Frequency spectra of the impellers with 150 and 228 degree wrap angle; simulation

Conclusion

The results extend the understanding of the flow field inside the impeller and the reason for noise generation. The code based on the Formulation I of Farassat of the FW-H's equation, using a stationary integration surface, provides good results which are matching well with experiment. Both, frequency peaks and overall sound pressure level could be predicted by the simulation in agreement with the experiment. Now, with the application of the acoustic solver the design of the impellers can be done concerning both, the aerodynamic and aeroacoustic processes. It turned out as well that hydrodynamic optimized machines will not automatically be acoustically optimized. Besides the aerodynamic optimization tool, aeroacoustic tools should also be applied in order to obtain the best efficient and the less noisy machine.

Acknowledgements

References

1 Becker, S., Hahn, C., Kaltenbacher, M., Lerch, R., 2008: "Flow-Induced Sound of Wall-Mounted Cylinders with Different Geometries", AIAA Journal, Vol. 46, No. 9, pp. 2265-2281

2 Ffowcs Williams, J.E., Hawkings, D.L., 1969: "Sound generation by turbulence and surfaces in arbitrary motion", Philosophical Transactions of the Royal Society of London A264, 321-342

3 Menter, F.R., 1993: "Zonal Two Equation k-w Turbulence Models for Aerodynamic Flows", AIAA Paper 93-2906

4 Bardina, J.E., Huang, P.G., Coakley, T.J., 1997: "Turbulence Modeling, Validation, Testing and Development", NASA Technical Memorandum 110446, (See also Bardina, J.E., Huang, P.G., Coakley, T.: "Turbulence Modeling Validation", AIAA Paper 97-2121)

5 Farassat, F., 1981: "Linear Acoustic Formulas for Calculation of Rotating Blade Noise", AIAA Journal, Vol. 19, No. 9, pp. 1122 - 1130

6 Di Francescantonio, P., 1997: "A New Boundary Integral Formulation for the Prediction of Sound Radiation", J. Sound Vib., Vol. 202, No. 4, pp. 491-509

7 Casalino, D., 2003: "An Advanced Time Approach for Acoustic Analogy Predictions", J. Sound Vib., Vol. 261, No. 4, pp. 583-612

8 Epple, P., Karic, B., Ilic, C., Becker, S., Durst, F., Delgado, A., 2009: "Design of Radial Impellers: a Combined Extended Analytical and Numerical Method", Proc. IMechE, Part C, J. Mechanical Engineering Science, 223(C4), pp. 901-917